

2 Improving grain size analysis using computer
3 vision techniques and implications for grain growth
4 kinetics

5 Isra S. Ezad^{1*}, Joshua F. Einsle², David P. Dobson¹, Simon A. Hunt³, Andrew
6 R. Thomson¹, John P. Brodholt¹

7 ¹Department of Earth Sciences, UCL, Gower Street, London, WC1E 6BT

8 ²School of Geographical and Earth Sciences, University of Glasgow, Glasgow, G12 8QQ

9 ³Department of Materials, University of Manchester, Sackville Street Building, Manchester, M1 3BB

10 **Abstract**

11 Earth's physical properties and mantle dynamics are strongly dependent on mantle grain size,
12 shape and orientation, these characteristics are however poorly constrained. Experimental
13 studies provide an opportunity to simulate the grain growth kinetics of mantle aggregates. The
14 experimentally determined grain sizes can be fit to the normal grain growth law ($G^n - G_0^n =$
15 $k_0 t \cdot \exp\left(\frac{-\Delta H}{RT}\right)$) and then be used to determine grain size throughout the mantle and geological
16 time. The grain growth dynamics of spinel – orthopyroxene mixtures in the upper mantle are
17 modelled here, by experimentally producing small grain sizes in the range of 0.5 to 2 μm radius
18 at pressures and temperatures equivalent to the spinel lherzolite stability field. To accurately
19 measure the sizes of these small grains we have developed a computer vision workflow; using

* Present address: Department of Earth and Environmental Sciences, Macquarie University, Balaclava Road, Sydney,

20 a watershed transformation which rapidly measures 68% more grains and produces a 20%
21 improvement in the average grain size accuracy and repeatability when compared with manual
22 methods. Using this automated approach, we have been able to identify a significant proportion
23 of small grains which have been overlooked when using manual methods. This additional
24 population of grains, when fit to the normal grain growth law, highlights the influence of
25 improved accuracy and sample size on the estimation of grain growth kinetic parameters. Our
26 results demonstrate that automatic computer vision enables a systematic, fast, repeatable
27 method of grain size analysis, across large data sets, improving the accuracy of experimentally
28 determined grain growth kinetics.

29 **Introduction**

30 Rocks are composed of large numbers of grains, or crystallites. A grain is formed of a coherent
31 continuous lattice, the boundary of which has a discontinuous change in crystal lattice or other
32 properties. The properties of these grains: their size, shape, orientation and how they interact,
33 influence the bulk properties of rocks. These aggregate properties influence many of Earth's
34 physical properties including strength or viscosity, and seismic anisotropy; these in turn impact
35 the large scale motion of plates and mantle overturns (Bercovici and Ricard 2013; Chu and
36 Korenaga 2012; Dannberg et al. 2017; Evans et al. 2001; Hirth and Kohlstedt 1995; Karato
37 1984; Yamazaki et al. 2010). On a smaller length scale, grain size is often used as the basis
38 for the classification of some igneous and clastic rocks, as well as interpretations of the
39 geological environment and the processes which formed it. Grain growth and recrystallisation
40 are active processes, continuously changing the grain size of mantle aggregates. This has far
41 reaching consequences, for example, the decoupling of the upper and lower mantle may be due
42 to a sudden grain size reduction associated with the spinel to perovskite transformation at the
43 660 km discontinuity (Dobson and Mariani 2014).

44 Interpreting indirect geophysical observations in terms of grain-size is extremely
45 difficult and therefore the aggregate grain-size of the mantle is poorly constrained. It is widely
46 thought to vary from millimeters to centimeters at ~400 km depth, close to the transition zone
47 (Faul and Jackson, 2005). Estimates of the lower mantle (depths > 660km) grain-size may vary
48 from 1 to 1000 μm (Solomatov et al. 2002; Solomatov and Reese 2008). Constraining the
49 evolution of grain size of the mantle by experiments is difficult because they are limited by
50 both extent, sample volume and result in small grain sizes tens of micrometers at most (Karato
51 1989; Kim et al. 2004; Faul and Jackson 2005; Yamazaki et al. 2005, 2010; Faul and Scott
52 2006; Nishihara et al. 2006; Hiraga et al. 2010b). The experimental pressure—temperature—
53 time series results are extrapolated over many orders of magnitude to mantle scales using
54 kinetic models (Hillert 1965; Chu and Korenaga 2012). These models assume the normal grain
55 growth law:

$$G^n - G_0^n = kt, \quad (1)$$

56 where G is grain size, G_0 the initial grain size, k rate constant, t time and n the grain growth
57 exponent. The rate constant, k , has an Arrhenius temperature dependence and a global fit can
58 be applied of the form:

$$(G^n - G_0^n) = k_0 t \cdot \exp\left(\frac{-\Delta H}{RT}\right), \quad (2)$$

61 where k_0 is the pre-exponential exponent, H the activation enthalpy for grain growth and R is
62 the gas constant.

63 Accurate simulation of grain growth under realistic mantle conditions and time frames
64 requires a very well constrained grain growth exponent (n). Determination of the grain growth
65 exponent for any set of experiments relies on accurate measurement of the grain size,
66 reproduced through annealing experiments. This requires imaging and analyzing of statistically
67 significant numbers of grains, often thousands, across multiple experiments. Ideally, the grain
68 measurements produce 2D log-normal distributions, which can describe normal grain growth

69 occurring in 3D space (Hillert 1965; Saetre 2002; Rios and Zöllner 2018) and kinetic grain
70 growth parameters (Burke and Turnbull 1952).

71 We examine a two-phase system spinel and orthopyroxene as an analogue to the
72 composition of the upper mantle. In grain growth experiments this two-phase system splits into
73 two compositionally distinct phases and grains ranging in size from roughly 0.5 μm to 2 μm .
74 These properties of the two phase system indicated that the most effective method for
75 measuring large volumes of grains from multiple samples is, back scatter electron, scanning
76 electron microscopy (BSE-SEM). This microscopic technique provides high spatial resolution,
77 with a contrast mechanism largely dominated by the average atomic mass of the material
78 examined. The experimental samples then image as bright spinel grains against a dark largely
79 uniform background of orthopyroxene. This high contrast system provides an excellent test
80 bed for developing automated techniques for detecting and measuring grains, especially when
81 the greater number of grains measured directly translates to an improved ability to estimate
82 kinetic parameters.

83 Manual measurement techniques such as the "intercept" (Mendelson 1969; Abrams
84 1971) and/or "areas of equivalent circles" methods still comprise a major technique for the
85 study of grain size. We focus on this comparison since a recent literature search shows the
86 "areas of equivalent circles" has been referenced 779¹ times in peer-reviewed scientific articles
87 within the last six years, whilst the "intercept method" has been referenced 602² times.
88 Furthermore, the common use of manual measurement for industrial applications is highlighted
89 by the published standard by ASTM International for the intercept method (ASTM E112-13
90 2012). This standard highlights the central problem with manual methods, low throughput of

¹ Number of articles was found using Scopus search, key words of "area of equivalent circles" and "grain size" were used in a search period between 2014-2020

² Number of articles was found using Scopus search, key words of "intercept" and "grain size" were used in a search period between 2014-2020

91 15 minutes per image for an expert analyst, and a large $\pm 16\%$ uncertainty in measured grain
92 sizes. For this study, manual grain size analysis of 30 sample images required over 7.5 hours
93 of expert level analysis time. Moreover, these analysis methods are more difficult for complex
94 samples with clustered grains or samples with complex grain shapes. There is therefore a clear
95 need for automated image processing as an alternative, faster, independent method of analysis
96 for grain size estimation from images.

97 As noted above the study here leverages the high contrast between spinel and
98 orthopyroxene with BSE-SEM microscopy to acquire sufficient 2D images for a log-normal
99 sample distribution. The computer vision methods developed here are general enough that they
100 can be applied and adapted to a wide range of other microscopic modalities, especially since
101 virtually all images collected these days are digital. Segmenting optical images follows largely
102 the same process as will be demonstrated below for BSE-SEM images. Likewise, the
103 challenges of segmenting three-dimensional X-Ray tomography data can be viewed as a
104 generalization of the methods presented here. Finally, microanalytical techniques such as
105 energy dispersive x-ray spectroscopy (EDS) or electron backscatter diffraction (EBSD) offer
106 methods for not only identifying grains but examining compositional or crystallographic
107 relationships in the mapped regions. It should be noted that these techniques record interactions
108 volumes compared to essentially the surface information of low-kV BSE imaging. This
109 interaction volume compromises some of the ultimate spatial resolution since the resulting EDS
110 or EBSD signal comes from volume of 0.75 to 1.0 μm at best. Further these techniques are
111 often an order of magnitude slower than BSE imaging due to the limitations of microanalytical
112 detectors.

113 Segmentation is a classical image processing approach used for the consistent and non-
114 subjective assignment of specific pixels to groupings within images. Advanced image
115 processing algorithms, including segmentation, are widely used across many scientific

116 disciplines, for image analysis problems at all scales and complexities (Soille and Ansoult
117 1990; Rossouw et al. 2015). However, these algorithms are seldom employed in geological
118 sciences (Barraud 2006; Wang 2007), despite accurate determination of grain size and textures
119 being paramount to our understanding of geological processes.

120 Inaccuracies and inefficiencies of manual image segmentation for grain-size analysis are
121 addressed here by, leveraging the open-source image processing Python libraries, hyperspy (de
122 la Peña et al. 2019) and scikit-image (van der Walt et al. 2014) implemented with interactive
123 Jupyter notebooks to deploy a *watershed segmentation workflow*. The watershed algorithm is
124 used here to pull spinel grains out of the background and isolate individual grains. This method
125 can be traced back to the 19th century (Maxwell 1870), through modifications in the 1980's
126 (Beucher 1982) to their current form in many segmentation procedures (Najman et al. 2011).

127 This computer vision approach improves grain size estimation by 20% via automatic
128 identification of individual and touching grains, prior to calculating their respective 2D grain
129 metrics, including area and center of mass. The sensitivity of the algorithm to local contrast
130 variations increases the overall number of particles measured, across the entire grain size
131 distribution, compared with manual user approaches. The robust workflow has minimal
132 research bias and processes entire data sets at a fraction of the time usually taken through
133 manual techniques alone. We test and apply the workflow to new grain growth kinetic
134 experiments on spinel-orthopyroxene aggregates relevant for xenolith exhumation rates. The
135 system investigated as part of this study is chemically simple and therefore imaging from SEM
136 methods was sufficient to produce many quality images for use with automated segmentation.

137

138 **Methods**

139 **High pressure experiments**

140 Grain growth experiments were performed on a 50:50 spinel-orthopyroxene mixture
141 picked from a natural spinel peridotite from Lanzarote (Carracedo et al. 1992; Neumann
142 et al. 1995; Bhanot et al. 2017) and ground under propanol to a starting grain size of around
143 0.1 μm . The use of a McCrone micronizing mill minimized crystal-structural damage,
144 whilst ensuring a uniform fine grain size which was important in ensuring that steady-state
145 grain growth was achieved rapidly during the annealing experiments. Experiments were
146 annealed at pressures and temperatures appropriate for the spinel lherzolite stability field
147 (1.2 – 1.65 GPa and 1323 - 1473 K) using a standard 18/11 multi-anvil cell assembly. Run
148 durations ranged from 2 - 120 hours and were performed using the multi-anvil apparatus
149 at University College London. All experimental conditions are reported in Table 1.

150 **Analytical techniques**

151 After temperature quench and overnight decompression, samples were recovered and set
152 in epoxy resin before polishing to the center of each capsule. Samples were polished to a
153 3 μm diamond finish providing a satisfactory finish for imaging of spinel grains, further
154 polishing was not possible as individual grains began to pull out leaving holes in the
155 sample (observed as black grain shaped regions in each of the sample micrographs in
156 Figure 1). Orthopyroxene grains appeared as large single crystals and poorly defined grain
157 boundaries (Figure 1), orthopyroxene was also more susceptible to polishing scratches
158 than spinel grains. The poorly defined grain boundaries and damaged surfaces of
159 orthopyroxene were not clearly visible enough to analyze as part of this study.
160 Fortuitously, due to the initial 50:50 ratio of spinel to orthopyroxene measuring just one
161 phase is sufficient to determine grain growth kinetics of the two-phase system.

162 Appropriate imaging of the samples is crucial to the success of any form of image
163 segmentation. 2D imaging techniques (scanning electron microscopy) were chosen for
164 time efficiency and a compromise between sample preparation and final image quality.

165 EBSD as discussed earlier is another popular 2D imaging technique but inappropriate for
166 the samples of this study, due to low throughput and preferential polishing of phases.
167 Chemical colloidal polishing increases surface topography on multi-phase samples of
168 varying hardness, resulting in poor mineral indexing.

169 Polished samples were imaged at UCL using the JEOL JSM – 6480LV scanning
170 electron microscope (SEM). The SEM was operated in backscattered electron imaging
171 mode (BSE) at 15 kV accelerating voltage and a beam current of approximately 10nA.
172 BSE imaging offers improved phase contrast compared with secondary electron imaging
173 since the scattering strength is a positive function of the mean atomic number and density.
174 Scattering intensity from surface roughness, scratches and local topography (such as polish
175 height difference between Spinel and Orthopyroxene) are minimized with BSE compared to
176 SE and EBSD. The high density and Fe- and Cr- enriched spinel grains have a high
177 scattering intensity compared to the lower density matrix phase. In cases where the spatial
178 resolution was not sufficient, additional higher-resolution imaging was conducted at
179 Cardiff University using the Zeiss Sigma HD Field Emission Gun Analytical SEM at 15kV
180 accelerating voltage, 120 μm aperture and 4 nA beam current.

181 A total of eleven high pressure experiments were conducted, with three temperature-
182 time series investigated throughout PT conditions appropriate to the spinel Lherzolite
183 stability field. Following high pressure, high temperature experiments, seven to fifteen
184 images per experiment were collected through SEM-BSE imaging. Images were taken at
185 different locations throughout the sample, to ensure any grain size variations due to thermal
186 gradients within the sample were accounted for. Example images are shown in Figure 1.
187 A total of 22 images, (two per experiment) were analyzed by automated segmentation,
188 whilst 30 images, (two to four per experiment) were analyzed manually, using the areas of
189 equivalent circles technique.

190 **Grain size estimation**

191 **Areas of equivalent circles**

192 Grain size was manually measured from multiple BSE images from each experiment
193 (Figure 1) using the NIH - Image J software package (Schneider et al. 2012). Each easily
194 identifiable spinel grain in an image was manually drawn around, with clumped regions
195 dissected into several grains. Image J was then used to determine the areas of each grain,
196 which were subsequently converted to apparent radii. Results of manual grain size analysis
197 are reported in Table 1.

198 Orthopyroxene grains though present at approximately the same ratio as spinel were
199 not analyzed for grain size, due to poor visibility of grain boundaries and susceptibility to
200 polishing artefacts e.g. scratches and holes (Figure 1). Orthopyroxene grains could not be
201 easily identified by researchers and therefore attempting to resolve its grain size was not
202 undertaken as part of this study.

203 This procedure is prone to user bias; complex grain geometries can be difficult to
204 accurately draw around, segmentation of clustered grains can involve arbitrary choices and
205 small grains can be systematically underrepresented. In order to investigate the
206 reproducibility between researchers, the images were analyzed using this method by two
207 "expert" investigators who previously agreed criteria for definition of individual grains
208 and segmentation. It was found between the two expert users that, on average, there was a
209 5 % difference in the average grain size measured on the same image, with a maximum
210 difference of 10 % in the measured grain size on the same image.

211 Standard error for all experiments ranged from 0.01-0.02 micrometers radius, for a
212 single expert investigator measuring grain size, except for E19-007, which has a much
213 larger standard error than all other experiments. The larger than expected standard error is
214 attributed to the morphology of grains in this experiment, which are more interconnected

215 than all the previous experiments (Figure 1 f), this makes determination of grain
216 boundaries more difficult and therefore segmenting grains for measurement is highly
217 uncertain. E19-007 was also separately imaged at UCL using a tungsten filament SEM,
218 resulting in a poorer quality image than the other experiments which were imaged via FE-
219 SEM at Cardiff University. Though grains are still highly visible against the background
220 matrix, the poorly defined boundaries and greater clumping of grains resulted in a larger
221 standard error. To ensure this standard error was representative and not due to
222 misinterpretation by the investigator, over 800 grains were analyzed from four separate
223 images each resulted with a large uncertainty on the average grain size.
224 This discrepancy is significantly larger than the standard error of the mean grain size for
225 an experiment so, to further explore this, datasets were fitted to the grain growth law
226 (Equation 2) using both the standard error from a single experimenter and a 5 % error as
227 alternative weighting schemes.

228 **Advanced image processing: watershed segmentation**

229 A watershed segmentation workflow has been developed to allow implementation of
230 user-independent reproducible measurements, which additionally increases the number of
231 grains measured in each individual image. The workflow is flexible enough to allow
232 analysis of multiple images from different experiments, which possess a range of grain
233 sizes and mineral contrasts as imaged under varying brightness and contrast settings and
234 across multiple instruments, all with minimum user intervention.

235 Our workflow is built in the open source language Python which provides access to
236 advanced image processing and microscopy libraries such as Scikit- Image and Hyperspy
237 (van der Walt et al. 2014; de la Peña et al. 2019). The workflow is implemented using
238 Jupyter Notebooks, providing an interactive method, not only for running the code, but
239 documenting the process and user decisions (Kluyver et al. 2016). The workflow is

240 available from GitHub details provided within supplementary materials. Our workflow,
241 not only produces a segmented binary image, but through a process of particle labeling
242 (built in function of Scikit-Image) can produce grain metrics for each individual object in
243 the image. The workflow follows the structure shown in Figure 2.

244 Following imaging by SEM all micrographs were converted from RGB to 8-bit
245 greyscale images, using the NIH-Image J software package (Schneider et al. 2012). This
246 maintains the greyscale range of the micrographs but presents them to the workflow in a
247 consistent data structure for analysis (Figure 2.1).

248 The entire watershed process seeks to accurately identify foreground objects (i.e.
249 grains) from the background, whilst additionally pulling apart touching grains. This is
250 accomplished through two iterations of the watershed process. The first defines the bright
251 grain basins against the dark background, while the second iteration seeks to pull apart
252 connected objects into individual grains.

253 Before initiating this process, the BSE greyscale intensity is normalized by assuming
254 the inherent noise in the image is approximately Gaussian. Imaging filters can then be used
255 quantitatively to denoise the greyscale intensity. For the BSE data in this report we
256 employed filters which amplify contrast gradients, while preserving the texture of the
257 image such as "total variation denoising" (TV) and "non-local means" (NLM) (Figure 2.2).
258 The TV filter is more successful with poor quality noisy images which require
259 amplification of the edge contrast e.g., sharpening in some areas whilst smoothing in the
260 background (Chambolle 2004). NLM provides a higher quality result but requires an initial
261 high quality dataset as, every pixel present is weighted based on the noise and normalized
262 (Buades et al. 2005). We apply both filters to every BSE image, and manually select which
263 filter has best preserved the grains of interest from the original image, whilst denoising the
264 data. For the purposes of this study the NLM filter was used for all experiments except

265 E19-007, which was imaged at UCL. It was determined that E19-007 was a lower quality
266 image than those produced by FE-SEM imaging and denoised most effectively by the TV
267 filter.

268 An initial watershed iteration identifies spinel grains sitting in a background matrix.
269 We define grain basins by taking the derivative of the denoised image using a Scharr filter,
270 which identifies boundaries or edges between grains and the background matrix by finding
271 the greyscale gradient (Figure 2.3a). We compute and report the Otsu threshold, a classical
272 segmentation tool, used for splitting image data which is bimodal (Yousefi 2015). Its
273 implementation does not capture all of the grains of interest, so we provide an initial seed
274 greyscale value, manually determined as 1.2 times the Otsu threshold. The watershed
275 algorithm then floods the grain basins of the Scharr image to define the maximum extent
276 of the bright foreground grains (Beucher 1994). This results in a binary overlay image of
277 lows (background = 0) and highs (grains = 1), which is used in combination with the
278 denoised greyscale image in subsequent processing steps.

279 Each of the foreground objects (preliminary interconnected grains) are labeled by
280 examining pixel connectivity. Preliminary metrics such as shape and size can be calculated.
281 At this stage the image still possesses pixels associated with bright specs and holes which
282 are artefacts of polishing. We remove the bright specs by manually cutting out pixels
283 corresponding to the highest 20 % greyscale intensity data from the processed image. Holes
284 are likewise addressed by applying morphological filters with Scikit- Image, extreme
285 values of the binarized image represent holes and are closed by specifying the smallest
286 number of pixels which represent the holes (van der Walt et al. 2014).

287 For the second watershed iteration (Figure 2.7) we cut apart interconnected grains in
288 the binary image by calculating the distance between grain edges and the center of a grain
289 basin. These distances define the secondary basins which are cut apart, by looking for

290 saddles in the distance map. Further, to minimize over-segmentation (which is a known
291 problem of watershed methods) we set a minimum distance to be considered (h-minima)
292 (Malpica et al. 1997). Distances below this threshold, of 2 pixels, are considered to be part
293 of a larger grain. This clearly marks where a boundary is required and the second
294 watershed algorithm is used to segment on the saddled regions only, thus separating
295 touching grains. Subsequent labeling of the individual grains allows for the automatic
296 calculation of particle metrics. These metrics can then be inspected in the Jupyter notebook
297 using Pandas data frames, or exported as a CSV file and explored using Excel (McKinney
298 2011). Reported metrics include the individual grain coordinates, grain area, eccentricity,
299 minimum and maximum axis lengths.

300 Overlaying the labeled image onto the original BSE micrograph provides a qualitative
301 method for the user to visually inspect the quality of the segmentation (Figures 2 and 3).
302 A single image can be processed in under 3 minutes using the workflow presented here, a
303 noticeable improvement in the efficiency of researchers compared to manual image
304 processing which can take up to 15 minutes per image (Campbell et al. 2018).

305 **Results**

306 An example of manual grain identification is shown in Figure 3 e, incomplete grains,
307 i.e. grains on the edges of BSE images, are ignored. The average grain size was determined
308 from grain size distributions for each experiment as reported in Figure 4.

309 Representative images of the watershed workflow are displayed in Figure 3, following
310 image processing each segmented image required a visual check to ensure grains had been
311 pulled apart appropriately in regions where clumping occurs, as well as removal of particle
312 metrics associated with grains on the edges of images e.g., partially visible grains. In some
313 images, very small particles were identified on the scale of a few (1-10) pixels, these tiny

314 particles were also removed from the particle metrics list as they represent objects below
315 the resolution of the SEM micrographs. Finally, clumped regions which had been
316 unsuccessfully segmented were manually removed as they skew the apparent grain size to
317 a larger average e.g., Figure 3, c. However, the under-segmented regions which were
318 removed were not significant compared to the number of grains identified and their removal
319 did not (2-7 %, reduction in total grains measured) change the determined average grain
320 size, within error.

321 After visual inspection and conversion of particle area to equivalent radii, a 2D grain
322 size distribution can be determined for each experiment and compared to those of hand-
323 picked grains (Table 1). Figure 4 shows grain size distributions for manual and automated
324 segmented analyses. Both manual and automated image processing procedures produce
325 log-normal grain size distributions, with the average grain size being a positive function
326 of temperature and time as expected (Hillert 1965; Atkinson 1988). Log-normal grain size
327 distributions are expected for normal grain growth, when estimating grain size from 2D
328 techniques, and provide a satisfactory solution describing grain growth in 3D space (Hillert
329 1965; Saetre 2002; Rios and Zöllner 2018). The resulting average grain size estimates from
330 both methods is provided in Table 1.

331 The watershed algorithm is able to uniquely identify more grains than the manual
332 approach for a given image, as shown in Figure 2. The grain size distribution plots (Figure
333 4) show that the tails of distributions from automated segmentation extend to smaller grain
334 sizes than manually segmented distributions. Additionally, the grain size distributions are
335 more complete across the entire range of measured sizes, demonstrating not only are
336 smaller grains missed from manual techniques but sampling across the entire distribution
337 is more accurate with the watershed algorithm.

338 The largest differences in average grain size between the two techniques are seen in

339 the longest duration experiments, suggesting smaller grains have not been identified by
340 manual techniques (Figure 4. a and c). Although, the grain size distribution is expected to
341 show an increased average number of large grains, the shape of these distributions should
342 remain almost constant for the relatively small experimental durations investigated here.
343 All experiments had a smaller average grain size when analyzed by automated techniques,
344 except for E16-088 and E16-085 (Figure 4.b), which increased in grain size by 0.9 μm and
345 0.3 μm , respectively. These two experiments were in fact conducted at the same PTt
346 conditions, 6 hours at 1373 K. It would be expected that their estimated average grain size
347 would agree within error, and whilst this is the case for a consistent method of analysis
348 (automated or manual), the grainsize increase by automated techniques may suggest over
349 segmentation by the user when cutting interconnected grains.

350 **Kinetic parameters for grain growth**

351 While this study is not primarily about the kinetic grain growth mechanisms of spinel-
352 orthopyroxene aggregates, calculated kinetic parameters can provide a valuable measure of
353 the quality of the estimated "average grain size". In addition, they are used to constrain the
354 grain growth mechanism and rate controlling species from many experimental grain
355 growth studies, and to extrapolate experimental datasets to geological timescales (Karato
356 1989; Yamazaki et al. 1996, 2005, 2010; Faul and Scott 2006; Nishihara et al. 2006; Hiraga
357 et al. 2010a).

358 A weighted non-linear least-squares fitting to the grain growth law expressed as $G =$
359 $[kt + G_0^n]^{1/n}$, was performed for each of the manual and watershed grain size
360 distributions. Grain size (G) was the dependent variable and an effective variance method
361 was used as the weighting scheme for the non-linear least-squares fitting. This weighting
362 scheme was chosen to reflect the uncertainty in both the dependent and independent

363 variables (Orear 1982), resulting in a more accurate solution to unknown parameters, and
364 error estimates closer to the true error which are commonly underestimated by minimizing
365 the weighted sum of the squared deviation.

366 A second fitting was performed with the additional 5 % error on the mean grain size
367 of manually analyzed grains, representing the inter-user error.

368 The grain growth exponent, n , is often expected to return a theoretical value of 2, where
369 normal grain growth is occurring in a simple single phase system (Hillert 1965). Polyphase
370 grain growth, is expected to yield values of 3, 4 or 5 for Zener-pinned grain growth, limited
371 by diffusion through the lattice, along grain boundaries or along line defects ("pipe
372 diffusion") respectively (Evans et al. 2001; Tsujino and Nishihara 2009).

373 The n values returned here range from 2.38 ± 0.12 to 4.15 ± 0.17 , implying a range of
374 coarsening processes may be operating. Aside from the grain growth exponent which may
375 be indicative of the rate limiting process, activation enthalpy is often considered a good
376 indicator of which species is rate limiting. The results from the regressions fall at values
377 between 297 ± 7.6 - 320 ± 11 kJ mol⁻¹.

378 The resulting kinetic parameters for manual and automated segmentation are reported
379 in Table 2.

380 **Discussion**

381 **Textural recovery**

382 Employing machine vision techniques, even in a supervised manner as demonstrated here,
383 provides a methodology for identifying complex anhedral grains. Figure 5 demonstrates the
384 watershed algorithm identifying clumped or touching grains while maintaining a visually
385 realistic morphology. Our workflow saves time by rapid analysis (under 3 minutes per
386 image), minimizes user bias and provides a consistent alternative to manual grain tracing

387 methods.

388 The watershed workflow has been successful in identifying grains from complicated
389 textures such as Figure 3 b. Many of the spinel grains exhibit bright chromium rich cores
390 with small rims of more aluminum rich spinel; these tend to dominate the shorter duration
391 experiments. The resulting texture is challenging to interpret as the contrast between the
392 background orthopyroxene and rims of spinel is small. However, the subtle difference in
393 greyscale, following the first watershed to remove the orthopyroxene background, is
394 sufficient to allow grains to be segmented from one another (Figure 3, d).

395 Our segmentation workflow has been calibrated for a multiphase system and therefore
396 takes advantage of bimodal greyscale intensities between the spinel and orthopyroxene
397 grains. Grain analysis in a single-phase system would in principle allow for the skipping
398 of the first watershed transform, since there is no background. This would be similar to the
399 Ti- α grains segmented in Campbell et al., (2009). For any single-phase system to be
400 successfully segmented there needs to be contrast between the grains. For some
401 polycrystalline materials this may not be apparent in BSE imaging, like the orthopyroxene
402 phase in our present experiments. To understand the grain structure of that phase other
403 more time intensive microscopy techniques would need to be considered such as EBSD.
404 This would allow for the mapping of grains based on variations in orientation. Ultimately,
405 the EBSD grain orientation data comes from an orientation map which needs to be
406 segmented based on the misorientation angle, which like any segmentation threshold is
407 user defined. Alternately, this data can be segmented using a watershed with threshold
408 examining from the disorientation distribution.

409 For cases where EBSD is clearly the superior technique, it should be noted that this
410 comes at a cost of throughput or spatial resolution. Wright (2010) highlights that to acquire
411 maps of just 250 grains via EBSD can take anywhere between 1.8 and 7.5 hours, dependent

412 on the age of the instrument and resolution required. Higher throughput could be achieved,
413 but for the spatial resolution required in these studies, the smallest grains would not be
414 resolved. Additionally, beam interaction effects would need to be considered (Wright
415 2010). It should also be noted that the samples in this study and in many geological systems
416 require uniform polishing for EBSD analysis which has proven to be challenging. For the
417 present samples, orthopyroxene preferentially polished with respect to spinel leaving
418 surface roughness which is unsuitable for EBSD analysis. For high throughput analysis of
419 multiphase systems where the absolute grain orientation is not a concern but statistically
420 meaningful grain size distributions are required BSE-SEM imaging becomes a preferable
421 cost-effective solution (Hillert 1965; Evans et al. 2001). SEM imaging in combination with
422 the segmentation workflow presented here, offers an excellent alternative for rapid
423 imaging and data analysis, which can all be achieved at a fraction of the time.

424 **Grain size distributions**

425 The tails on grain size distributions from manual methods, (Figure 4) demonstrate user bias
426 to systematically picking larger grains and ignoring smaller ones. Subtle changes in
427 greyscale within SEM micrographs mask smaller grains which are difficult to uniquely
428 differentiate from the inherent noise within images. Providing a minimum pixel size for
429 the smallest truly "visible" grain within the resolution of SEM micrographs, reduces the
430 number of very small grains sampled in the automated segmentation approach, as can be
431 seen in the left-hand sides of Figure 4 a and c.

432 As well as identifying a greater number of small grains from images, automated
433 segmentation is also more representative of the "average" grain size. This is clearly
434 demonstrated by greater sampling of grains across the entire distribution, not just at
435 extreme small grain size values, as shown in Figure 4. Thus, the adjustment of average
436 grain size to smaller values is not exclusively related to increased sampling of small grains;

437 as there is an increase in grain identification and sampling across the whole distribution.
438 Further suggesting the average grain size from manual techniques is misrepresentative of
439 the distribution due to under sampling across the whole distribution.

440 The greatest discrepancies in average grain size were seen in experiments with the
441 largest grain sizes, corresponding to longer duration experiments and higher temperatures.
442 This may be due to the systematic over picking of large grains by the user, during the
443 image-analysis stage, using the areas of equivalent circles technique. This shifting of the
444 average grain size to large values has consequences for the interpretation of grain growth
445 kinetics, determined from these values.

446 The mean grain size was estimated from the grain size distributions and it was
447 found that both techniques returned a similarly small standard error on the mean grain
448 size for a measured population. Importantly, the discrepancy of the larger than
449 expected standard error for E19-007 from manual techniques, is now within the range
450 of values from automated techniques, implying better sampling and accurate error
451 determination from automated techniques. The difference in mean grain size between
452 the two independent expert investigators was found to be approximately 5 % of the mean
453 grain size, some two to ten times greater than the formal error. This discrepancy was
454 found to be even larger when comparing results from inexperienced (third-year
455 undergraduate) investigators. Even with a small 5 % error between users, this can lead to
456 substantially different grain growth kinetics and thereby grain growth mechanism, as will
457 be shown below.

458 **Grain growth kinetics**

459 All the values of n obtained through the two methods of grain size analysis are theoretically
460 possible for a system of polyphase grain growth, suggesting grain growth in this system is
461 Zener-pinned and limited by diffusion along grain boundaries or through the lattice. Values

462 are also consistent with observations from grain growth studies in other upper mantle
463 phases, for example Hiraga et al., (2010) who conducted grain growth experiments on
464 forsterite-enstatite aggregates and found n values ranging between 3 and 5, for a consistent
465 method of grain size analysis and varying proportions of their secondary phase, enstatite.
466 Our n values fall within a similar range, suggesting these are typical values of upper mantle
467 phases (Figure 6). However, we find a very large difference in n between the manual and
468 automated methods (2.38 and 4.15 respectively). This difference would be interpreted as
469 different mechanisms, either interface diffusion or grain boundary diffusion (Evans et al.
470 2001; Kim et al. 2004). Either case has a different grain growth exponent and could imply
471 a variety of diffusive mechanisms may be responsible for the rate limiting step.

472 This disparity between kinetic solutions for the two analysis methods is however
473 reduced, when the formal error on the average grain size is modified to 5 % of the mean
474 grain size (Table 2). Most influential to the determined kinetic parameters is the treatment
475 of E19-007, as the grain growth exponent is effectively pinned by the longest duration
476 experiment. Manual techniques consistently underestimate the standard error, whilst
477 automated approaches result in larger and perhaps more realistic formal errors. By
478 accommodating the true errors on manual measurement approaches, the grain growth
479 exponent is more consistent to higher values of n , (3.47 ± 0.23 to 4.15 ± 0.17). Yet these
480 values still imply very different dominant diffusive mechanisms and an averaged grain
481 growth exponent for the system based on both techniques, would be subject to large
482 uncertainties and makes determining the grain growth mechanism troublesome.

483 But more importantly, large uncertainties in n also reduces the possibility of accurately
484 extrapolating grain size through time. The small variations in the grain growth exponent
485 here, lead to differences of greater than 25 % in the predicted grain size at only 14 days
486 (Figure 6). This difference is even more pronounced when assuming the initial errors on

487 the mean grain size from manual approaches are accurate. The divergence of predicted
488 grain size increases with time, and eventually the confidence intervals overlap across
489 widely different temperatures (Supplementary Figure 1). The problem of large
490 uncertainties in the grain growth exponent is often dealt with by fixing n for the purposes
491 of extrapolation (Yamazaki et al. 2005; Nishihara et al. 2008; Hiraga et al. 2010a).
492 However, as shown here even small uncertainties in n significantly alter extrapolated grain
493 sizes through time, as well as potentially changing interpretation of the grain growth
494 mechanism. Thus, fixing n , to possibly the wrong value, will produce misleading
495 predictions. Making interpretations on the grain growth mechanism and extrapolated grain
496 size subject to large unconstrained uncertainties.

497 Despite the challenges in evaluating grain size through time, the activation enthalpy
498 from the manual + 5 % error approach, almost agrees within error of the automated
499 solution at 278 ± 19 - 320 ± 11 kJ mol⁻¹, respectively. This suggests Fe-Mg diffusion in
500 orthopyroxene may be the rate limiting step in coarsening of this two phase spinel-
501 orthopyroxene system (Dohmen et al. 2016). The prediction of the same rate limiting
502 species, by both methods of analysis, suggests a significant amount of time has passed and
503 the rate limiting species now has an influence on coarsening of the system. Dohmen et al.,
504 (2016) measured the interdiffusion coefficients of Fe-Mg in orthopyroxene, which takes
505 place through lattice diffusive mechanisms, whilst the activation enthalpy now agrees
506 within error of their estimates (308 ± 23 kJ mol⁻¹), a grain growth exponent of 3 would be
507 expected in the case of lattice diffusion. Both methods of analysis return grain growth
508 exponents greater than 3, demonstrating the challenge in accurately determining both the
509 rate limiting mechanism and species.

510 Although the kinetic solutions presented here are subject to large uncertainties,
511 automated segmentation still presents the most satisfactory interpretation of spinel grain

512 growth. We do not report further predictions on grain size through geological time for the
513 reasons discussed above. Further investigations are required to determine the accuracy of
514 grain size and its eventual use to constrain grain growth kinetics, caution is emphasized
515 when using small experimental data sets to constrain such kinetic parameters as has been
516 commonplace for many grain growth studies (Hiraga et al., 2010; Nishihara et al., 2004;
517 Tsujino and Nishihara, 2010; Yamazaki et al., 2010, 2005, 1996).

518 Large uncertainties, such as the ones reported here, are common within grain growth
519 studies focused solely on image analysis (Yamazaki et al. 1996, 2005, 2009; Nishihara et
520 al. 2006; Hiraga et al. 2010a). This demonstrates the need to go beyond only collecting
521 SEM-BSE data. Combining grain size measurements with analytical techniques like
522 energy dispersive spectroscopy, electron back-scattered diffraction or high resolution 3D
523 X-ray micro tomography would unlock important information about the mechanisms for
524 grain growth. Using correlative and machine learning approaches, all these datasets can
525 be combined to form quantitative statistical descriptions of the grain growth kinetics
526 (Einsle et al. 2018).

527 **Implications**

528 The automated watershed workflow presented here appears to improve the reproducibility
529 of grain size measurements while increasing the yield of grains measured compared to
530 traditional manual approaches. This workflow demonstrates a clear advantage in the
531 minimization of user bias, but many of the parameters required manual tuning to produce
532 an optimal "realistic" measurement. Additionally, the speed at which datasets can be
533 analyzed is greatly enhanced with the use of automated techniques.

534 One of the biggest areas of active research relates to the use of machine learning and
535 artificial intelligence to improve the segmentation of images. These data driven approaches

536 offer further advantages in that the segmentation criteria become defined by examining the
537 statistics of an image set and looking at variations of different image filters applied to the
538 same image. This works particularly well when examining tomographic data sets
539 generated by micro CT or FIB-SEM tomography techniques. Great progress has recently
540 been made applying clustering or neural network techniques to these large data sets
541 (Andrew 2018). Clustering analysis may offer the best path forward for small data sets like
542 the ones presented here. Tomographic imaging, by contrast, produces data sets with
543 hundreds to thousands of images, offering the most advantage for supervised machine
544 learning tools. With the rise in automated mapping techniques, it should be possible to
545 collect large numbers of BSE images across an entire thin section, or collections of
546 sections. Batch processing would benefit from supervised machine learning enabled
547 workflows.

548 The rapid collection of large volumes of data would result in better estimates of grain size
549 and therein grain growth kinetics. To this end, and to further the implementation of
550 automated segmentation and facilitate improvements in grain size estimation, there needs
551 to a community move towards greater data sharing and accesses as has been advocated for
552 within the geological sciences community (Stall et al. 2019).

553 We have highlighted systematic biases in interpreting grain size from 2D images including;
554 the exclusion or misinterpretation of small grains by traditional analysis techniques
555 alongside grain size distributions misrepresentative of the mean grain size.

556 The automated workflow described here can therefore significantly improve grain size
557 distributions by accounting for missing data, across the entire distribution. We
558 acknowledge the challenges in extrapolating grain size to geological time and present a
559 first attempt to address this problem by improving grain size analysis. Additionally we

560 present a kinetic solution to the grain growth of spinel-orthopyroxene aggregates, which
561 represents coarsening of a two phase system, limited by Mg lattice diffusion in
562 orthopyroxene (Dohmen et al. 2016). To address the uncertainties in experimentally
563 determined grain growth exponents, much longer duration annealing experiments are
564 required, beyond those usually possible in high pressure, high temperature apparatus. It is
565 for this reason that the data, which is available, must be treated in a systematic,
566 reproducible manner. As demonstrated here, small changes in only the reported 1 ϵ -errors
567 can lead to misinterpretations of the grain growth kinetics. However further improvements
568 are needed in the determination of experimental grain sizes before kinetic solutions can be
569 applied to the Earth.

570 We have demonstrated our segmentation workflow is able to rapidly process multiple
571 SEM images in a consistent and repeatable manner, from an initial complex grayscale
572 image. Automated segmentation vastly increases the number of grains identified and
573 indexed per 2D image, as compared to expert researchers analyzing the same images (see
574 Table 1). The number of grains identified and indexed by automated segmentation shows
575 an impressive 68 % increase as compared to manual techniques alone (7264 grains
576 compared to 4314). This alone, demonstrates the power of utilizing computer vision for
577 grain analysis and also results in a coherent kinetic solution.

578 **Acknowledgements**

579 We thank James Davy for assistance with SEM imaging at UCL and Duncan Muir for
580 imaging at Cardiff University. The ‘inexpert investigators’ were third-year undergraduate
581 students at UCL (GEOL0039; 2018-19 cohort). We thank two anonymous reviewers for
582 their comments, which helped improve this manuscript and Bin Chen for their editorial
583 handling. This work was part of ISE’s NERC-funded Ph.D (award NE/M00046X/1 to JB

584 and DD). JFE acknowledges funding under ERC Advanced Grant 320750-
585 Nanopaleomagnetism.

Accepted revision

Experimental run	P (GPa)	T (K)	Time (h)	Manual		Watershed	
				Average grain size (μm)	No. identified	Average grain size (μm)	No. identified
E17 - 050	1.2	1323	6	0.46 (0.01)	325	0.41 (0.01)	603
E17 - 053	1.2	1323	25	0.63 (0.01)	239	0.47 (0.01)	525
E17 - 059	1.2	1323	48	0.65 (0.01)	299	0.50 (0.01)	678
E17 - 016	1.2	1373	2	0.39 (0.01)	353	0.37 (0.02)	686
E16 - 088	1.4	1373	6	0.50 (0.02)	450	0.59 (0.01)	647
E16 - 085	1.2	1373	6	0.47 (0.02)	503	0.50 (0.09)	578
E18 - 003	1.4	1373	24	0.74 (0.02)	250	0.64 (0.01)	286
E17 - 017	1.65	1473	3	0.63 (0.02)	323	0.51 (0.01)	434
E17 - 018	1.65	1473	6	0.78 (0.02)	219	0.61 (0.03)	749
E16 - 090	1.65	1473	18	1.30 (0.01)	492	0.89 (0.01)	975
E19 - 007	1.65	1473	120	1.74 (0.20)	861	1.30 (0.03)	1103

586 Table 1: Experimental run conditions and results from area of equivalent circles method, Python automated segmentation workflow. All
587 grain sizes are reported as radii, values in parenthesis are one standard error on the mean grain size.

588

589

Measurement Method	Log k_0	ΔH ($kJmol^{-1}$)	n	$G_0(\mu m)$
Manual	$10^{5.61 \pm 5.43}$	287 ± 7.6	2.38 ± 0.12	0.37 ± 0.01
Manual + 5% error	$10^{5.15 \pm 5.37}$	278 ± 19	3.47 ± 0.23	0.30 ± 0.05
Watershed	$10^{6.27 \pm 6.23}$	320 ± 11	4.15 ± 0.17	0.38 ± 0.01

590

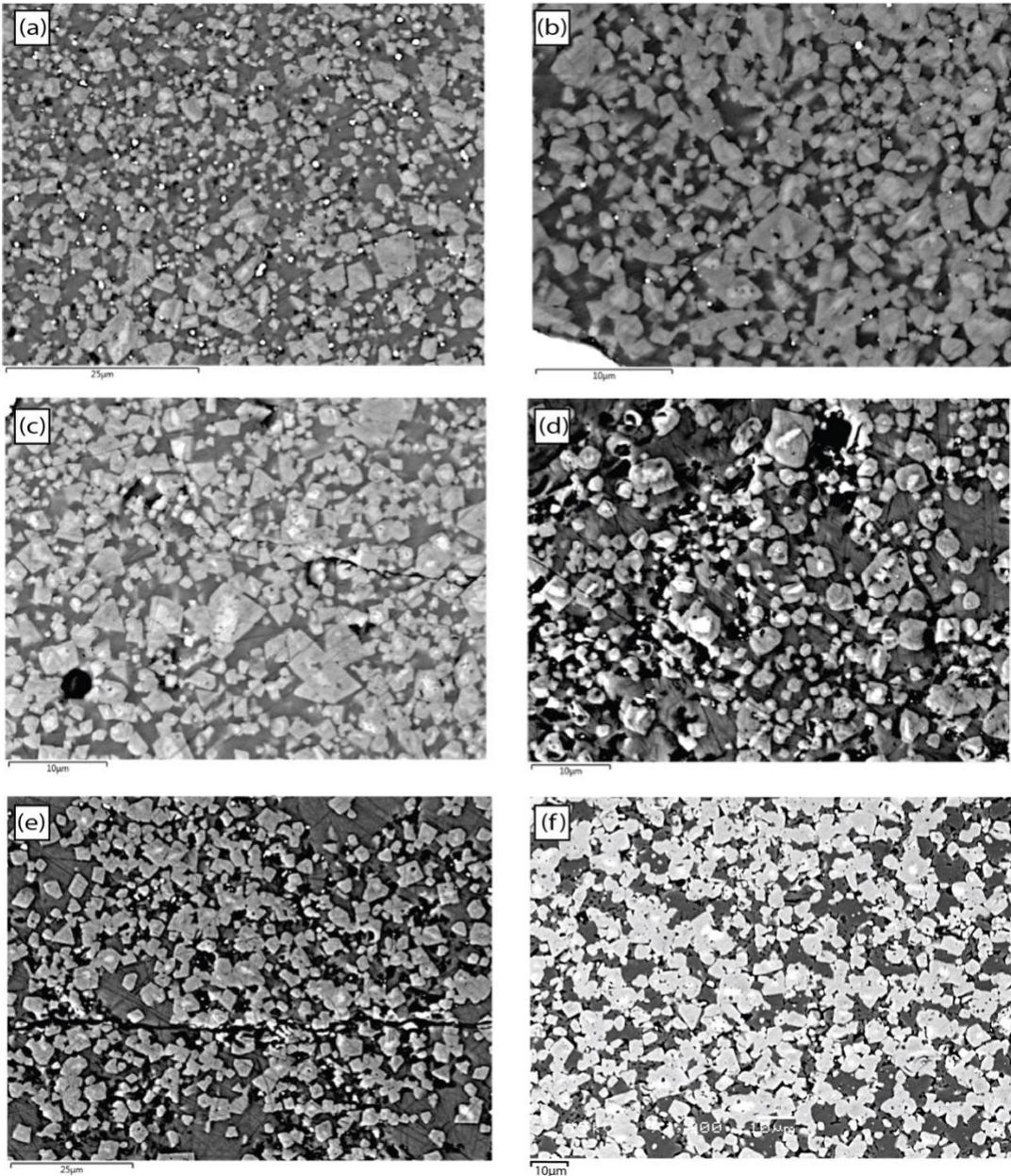
591 Table 2: Kinetic grain growth parameters returned from non-linear least- squares

592 fitting, to all experimental data.

593

594

Accepted revision



595

596

597

598

599

600

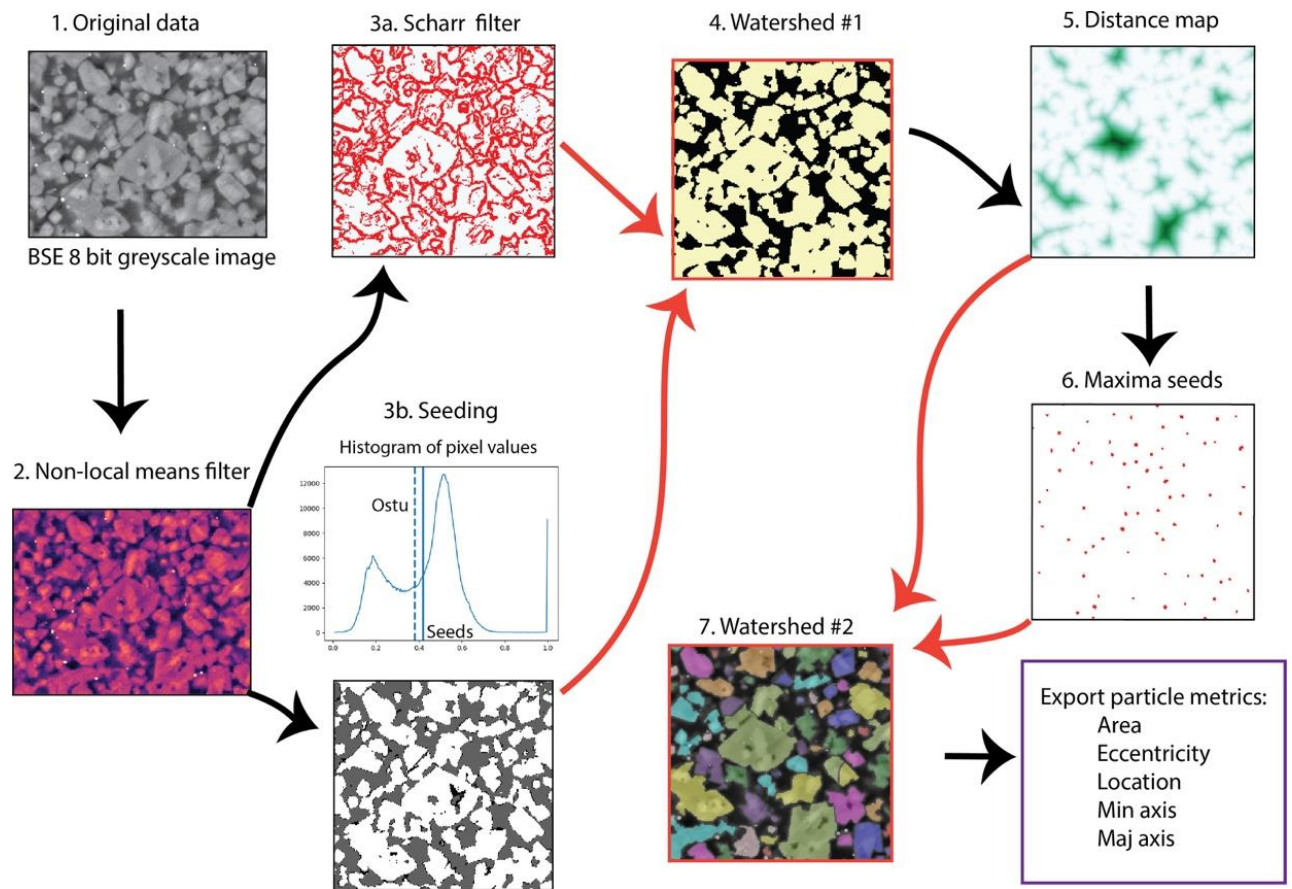
601

602

603

Figure 1: BSE micrographs of recovered high PT experiments, (a) E17-050 (1323 K, 6 hours). (b) E17-053 (1323 K, 25 hours) (c) E17-016 (1373 K, 2 hours) (d) E17-018 (1473 K, 6 hours) (e) E16-090 (1323 K, 18 hours) (f) E19-007 (1373 K, 120 hours). Micrographs are ordered in increasing experimental temperature and duration. For complete run conditions see Table 1. Spinel grains are clearly visible as euhedral to subhedral grains with bright chromium cores. The matrix material is orthopyroxene +/- clinopyroxene, dependent on the initial composition of the starting material.

604
605



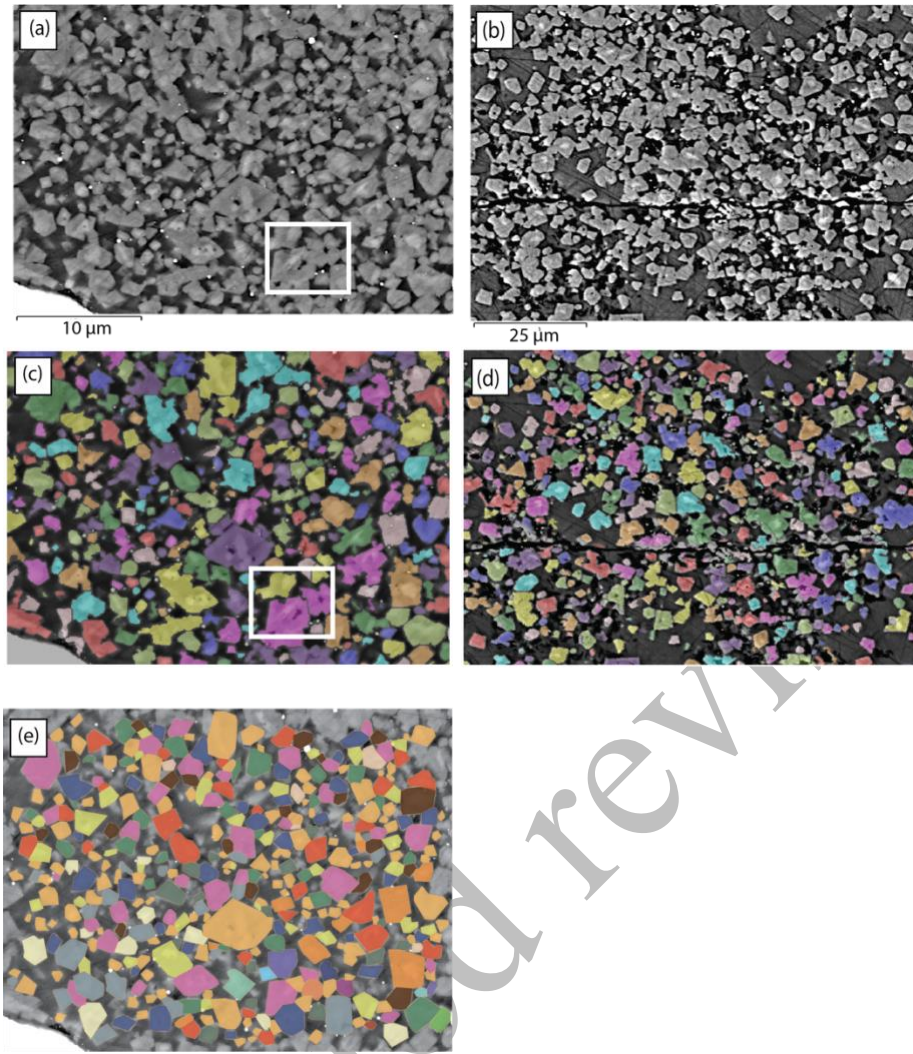
606
607
608

609 Figure 2: A simplified diagrammatic workflow of the image processing code
610 developed for the analysis of spinel grain growth experiments. Images are first
611 loaded in an 8-bit greyscale format and image processing filters are used to denoise
612 the original image. In step 3, a Scharr filter is applied to identify grains. Step 4
613 pulls these away from the background matrix with the use of watershed A. At the
614 same time an additional step is added to remove bright specks and fill in any holes
615 present within the image. Step 5, interconnected grains are identified by peaks and
616 basins in the greyscale intensity and shown as a distance map. Grain locations are
617 highlighted by seeds and their positions represent the peaks in greyscale intensity,

618 i.e. this corresponds to the center of grains. In combination with the distance map
619 at step 7 watershed B is implemented to pull apart interconnected grains from one
620 another and the final result is overlain onto the original BSE image for a visual end
621 result. The addition of color in step 7 is arbitrary and used to overlay segmented
622 grains onto the original BSE image for visual inspection.

623
624
625
626
627
628
629
630
631
632
633

Accepted revision



634

635

636

637

638

639

640

641

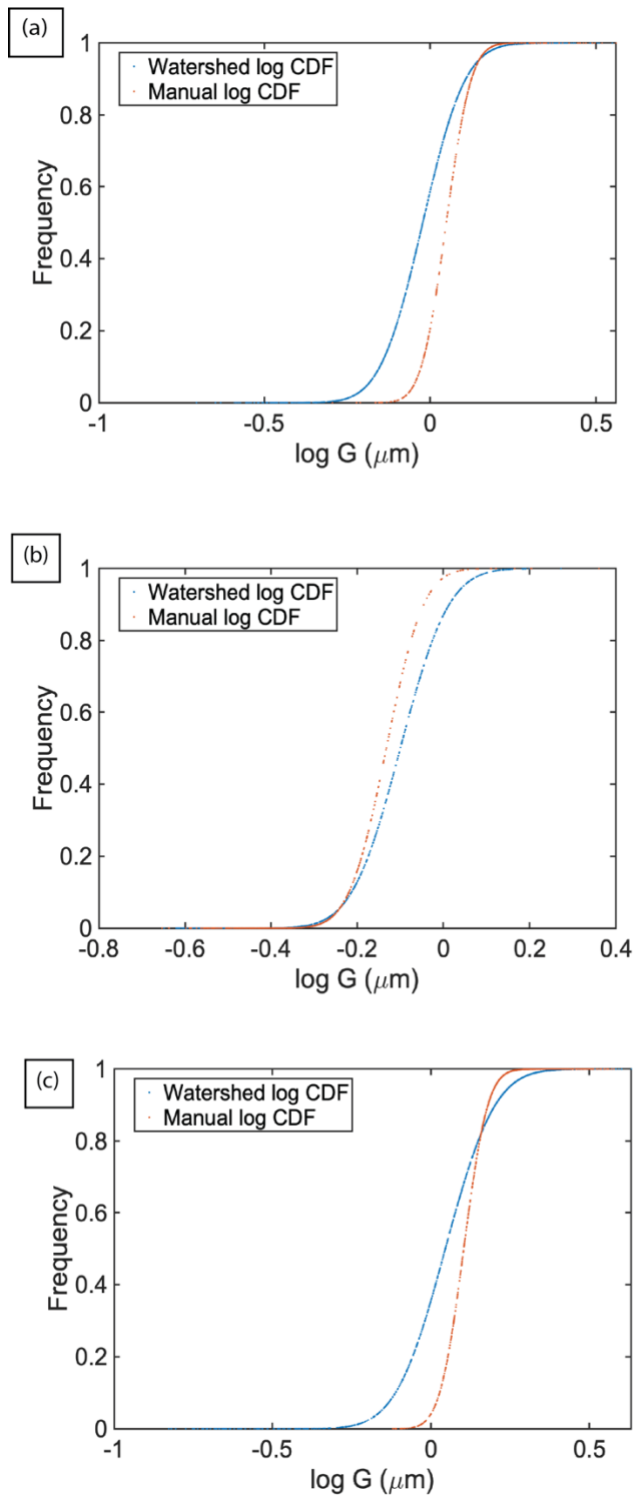
642

643

644

645

Figure 3: BSE micrographs from experiments (a) E17-053 and (b) E16-090. with their associated segmented images produced from the Python workflow below (c, d). The colored regions in c and d represent singular grains identified by the code. The majority of images are segmented, visually, well but regions of under-segmentation exist. The white highlighted region in c shows multiple grains which have been clumped together and interpreted as a single grain. (e) is an example of visually identified and hand-drawn grains using the NIH image - J software package.



CVISION

646

647

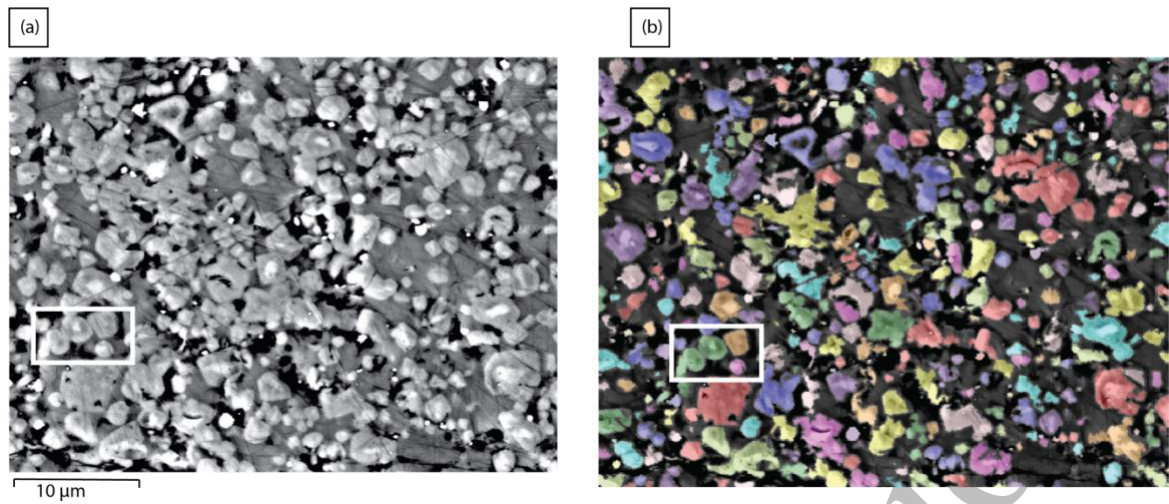
648 Figure 4: Log-normal distributions for user-analyzed grain sizes in orange and

649 automated image segmentation in blue. (a) E16-090, (b) E16-088 and (c) E19-007.

650

651

652



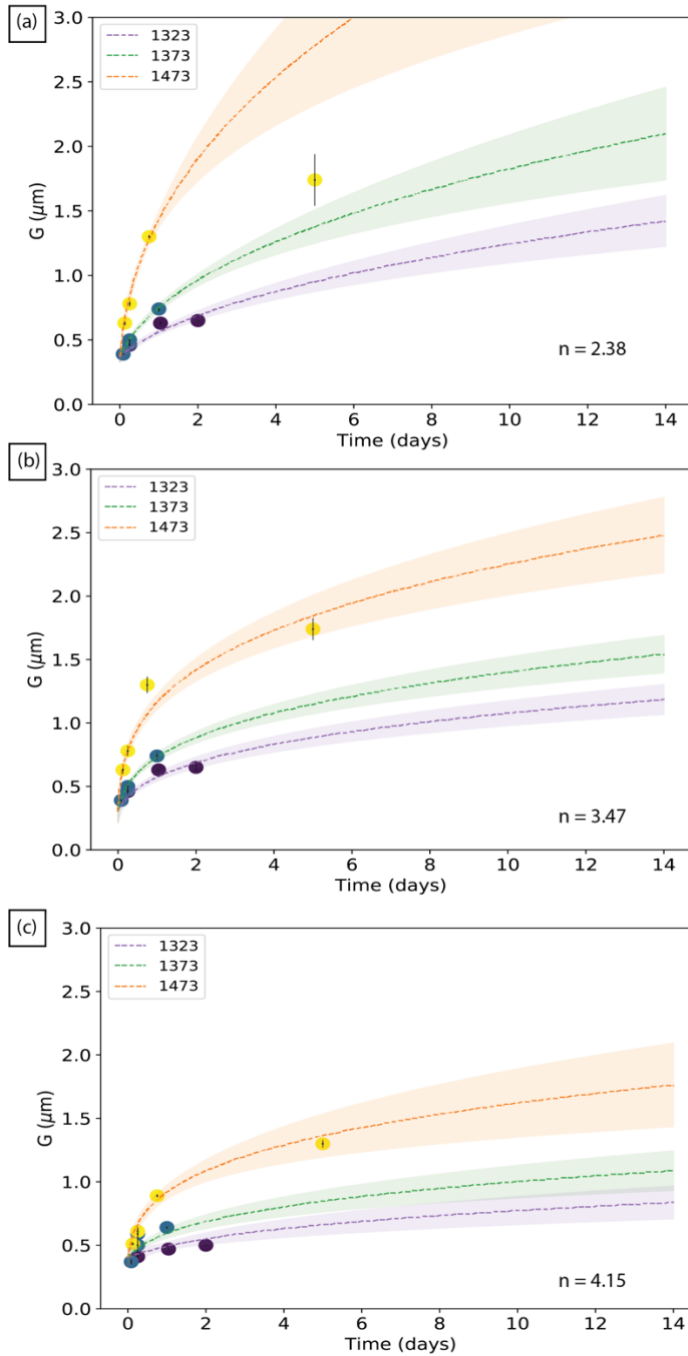
653

654 Figure 5: (a) SEM micrograph of E17-018 with its' segmented image in (b).

655 Regions highlighted in white boxes demonstrate the ability of automated image

656 segmentation to pull apart clumped grains whilst retaining their morphology.

Accepted revision



CVISION

657

658 Figure 6: A global fit of grain size to the normal grain growth law, with expected
 659 95 % confidence intervals for a period of 14 days. (a) Best fit solution from manual
 660 segmentation. (b) A fit to the grain growth law following image analysis from
 661 manual segmentation and an additional 5 % error, amongst multiple users. (c) The
 662 best fit solution for grain size estimated from automated watershed segmentation.
 663 n is the best fitting grain growth exponent for each data set.

664 **References**

- 665 Abrams, H. (1971) Grain Size Measurements by the Intercept Method. *Metallography*, Vol.
666 4, 59-78.
- 667 Andrew, M. (2018) A quantified study of segmentation techniques on synthetic geological
668 XRM and FIB-SEM images. *Computational Geosciences*, 22, 1503–1512.
- 669 ASTM E112-13 (2012) Standard Test Method for Determining Average Grain Size. ASTM
670 International.
- 671 Atkinson, H. V. (1988) Overview no. 65. Theories of normal grain growth in pure single
672 phase systems. *Acta Metallurgica*, 36, 469–491.
- 673 Barraud, J. (2006) The use of watershed segmentation and GIS software for textural analysis
674 of thin sections. *Journal of Volcanology and Geothermal Research*, 154, 17–33.
- 675 Bercovici, D., and Ricard, Y. (2013) Generation of plate tectonics with two-phase grain-
676 damage and pinning: Source-sink model and toroidal flow. *Earth and Planetary Science*
677 *Letters*, 365, 275–288.
- 678 Beucher, S. (1982) Watersheds of functions and picture segmentation. *ICASSP, IEEE*
679 *International Conference on Acoustics, Speech and Signal Processing - Proceedings*,
680 1982-May, 1928–1931.
- 681 ——— (1994) Watershed, Hierarchical Segmentation and Waterfall Algorithm pp. 69–76.
- 682 Bhanot, K.K., Downes, H., Petrone, C.M., and Humphreys-Williams, E. (2017) Textures in
683 spinel peridotite mantle xenoliths using micro-CT scanning: Examples from Canary
684 Islands and France. *Lithos*, 276, 90–102.
- 685 Buades, A., Coll, B., and Morel, J.M. (2005) A non-local algorithm for image denoising.

686 Proceedings - 2005 IEEE Computer Society Conference on Computer Vision and
687 Pattern Recognition, CVPR 2005, II, 60–65.

688 Burke, J.E., and Turnbull, D. (1952) Recrystallization and grain growth. *Progress in Metal*
689 *Physics*, 3, 220–292.

690 Campbell, A., Murray, P., Yakushina, E., Marshall, S., and Ion, W. (2018) New methods for
691 automatic quantification of microstructural features using digital image processing.
692 *Materials and Design*, 141, 395–406.

693 Campbell, A.J., Danielson, L., Richter, K., Seagle, C.T., Wang, Y., and Prakapenka, V.B.
694 (2009) High pressure effects on the iron-iron oxide and nickel-nickel oxide oxygen
695 fugacity buffers. *Earth and Planetary Science Letters*, 286, 556–564.

696 Carracedo, J.C., Rodriguez Badiola, E., and Soler, V. (1992) The 1730-1736 eruption of
697 Lanzarote, Canary Islands: a long, high-magnitude basaltic fissure eruption. *Journal of*
698 *Volcanology and Geothermal Research*, 53, 239–250.

699 Chambolle, A. (2004) An Algorithm for Total Variation Minimization and Applications.
700 *Journal of Mathematical Imaging and Vision*, 20, 89–97.

701 Chu, X., and Korenaga, J. (2012) Olivine rheology, shear stress, and grain growth in the
702 lithospheric mantle: Geological constraints from the Kaapvaal craton. *Earth and*
703 *Planetary Science Letters*, 333–334, 52–62.

704 Dannberg, J., Eilon, Z., Faul, U., Gassmüller, R., Moulik, P., and Myhill, R. (2017) The
705 importance of grain size to mantle dynamics and seismological observations.
706 *Geochemistry, Geophysics, Geosystems*, 18, 3034–3061.

707 de la Peña, F., Prestat, E., Fauske, V.T., Burdet, P., Jokubauskas, P., Nord, M., Ostasevicius,
708 T., MacArthur, K.E., Sarahan, M., Johnstone, D.N., and others (2019, September 6)

709 hyperspy/hyperspy: HyperSpy v1.5.2.

710 Dobson, D.P., and Mariani, E. (2014) The kinetics of the reaction of majorite plus
711 ferropericlasite to ringwoodite: Implications for mantle upwellings crossing the 660 km
712 discontinuity. *Earth and Planetary Science Letters*, 408, 110–118.

713 Dohmen, R., Ter Heege, J.H., Becker, H.W., and Chakraborty, S. (2016) Fe-Mg
714 interdiffusion in orthopyroxene. *American Mineralogist*, 101, 2210–2221.

715 Einsle, J.F., Martineau, B., Buisman, I., Vukmanovic, Z., Johnstone, D., Eggeman, A.,
716 Midgley, P.A., and Harrison, R.J. (2018) All Mixed Up: Using Machine Learning to
717 Address Heterogeneity in (Natural) Materials. *Microscopy and Microanalysis*, 24, 562–
718 563.

719 Evans, B., Renner, J., and Hirth, G. (2001) A few remarks on the kinetics of static grain
720 growth in rocks. *International Journal of Earth Sciences*, 90, 88–103.

721 Faul, U., and Jackson, I. (2005) The seismological signature of temperature and grain size
722 variations in the upper mantle. *Earth and Planetary Science Letters*, 234, 119–134.

723 Faul, U.H., and Scott, D. (2006) Grain growth in partially molten olivine aggregates.
724 *Contributions to Mineralogy and Petrology*, 151, 101–111.

725 Hillert, M. (1965) On the theory of normal and abnormal grain growth. *Acta Metallurgica*,
726 13, 227–238.

727 Hiraga, T., Tachibana, C., Ohashi, N., and Sano, S. (2010a) Grain growth systematics for
728 fosterite + enstatite aggregates: Effect of lithology of grain size in the upper mantle. *Earth
729 and Planetary Science Letters*, 291, 10–20.

730 Hiraga, T., Miyazaki, T., Tasaka, M., and Yoshida, H. (2010b) Mantle superplasticity and its

731 self-made demise. *Nature*, 468, 1091–1094.

732 Hirth, G., and Kohlstedt, D.L. (1995) Experimental constraints on the dynamics of the
733 partially molten upper mantle: 2. Deformation in the dislocation creep regime. *Journal*
734 *of Geophysical Research: Solid Earth*, 100, 15441–15449.

735 Karato, S. (1989) Grain growth kinetics in olivine aggregates. *Tectonophysics*, 168, 255–273.

736 Karato, S.I. (1984) Grain-size distribution and rheology of the upper mantle. *Tectonophysics*,
737 104, 155–176.

738 Kim, B.N., Hiraga, K., and Morita, K. (2004) Kinetics of normal grain growth depending on
739 the size distribution of small grains. *Nippon Kinzoku Gakkaishi/Journal of the Japan*
740 *Institute of Metals*, 68, 913–918.

741 Kluyver, T., Ragan-kelley, B., Pérez, F., Granger, B., Bussonnier, M., Frederic, J., Kelley,
742 K., Hamrick, J., Grout, J., Corlay, S., and others (2016) Jupyter Notebooks—a
743 publishing format for reproducible computational workflows. *Positioning and Power in*
744 *Academic Publishing: Players, Agents and Agendas*, 87–90.

745 Malpica, N., De Solórzano, C.O., Vaquero, J.J., Santos, A., Vallcorba, I., García-Sagredo,
746 J.M., and Del Pozo, F. (1997) Applying watershed algorithms to the segmentation of
747 clustered nuclei. *Cytometry*, 28, 289–297.

748 Maxwell, J.C. (1870) On hills and dales. *The London, Edinburgh, and Dublin Philosophical*
749 *Magazine and Journal of Science*, 40, 421–427.

750 McKinney, W. (2011) pandas: a Foundational Python Library for Data Analysis and
751 Statistics. *Conference Proceedings*.

752 Mendelson, M.I. (1969) Average Grain Size in Polycrystalline Ceramics. *Journal of the*

753 American Ceramic Society, 52, 443–446.

754 Najman, L., Couprie, M., Bertrand, G., Najman, L., Couprie, M., and Watersheds, G.B.
755 (2011) Watersheds , mosaics and the emergence paradigm To cite this version : HAL
756 Id : hal-00622113. Discrete Applied Mathematics, 147, 301–324.

757 Neumann, E.R., Wulff-Pedersen, E., Johnsen, K., Andersen, T., and Krogh, E. (1995)
758 Petrogenesis of spinel harzburgite and dunite suite xenoliths from Lanzarote, eastern
759 Canary Islands: Implications for the upper mantle. Lithos, 35, 83–107.

760 Nishihara, Y., Takahashi, E., Matsukage, K.N., Iguchi, T., Nakayama, K., and Funakoshi, K.
761 (2004) Thermal equation of state of $(\text{Mg}_{0.91}\text{Fe}_{0.09})_2\text{SiO}_4$ ringwoodite. Physics of the
762 Earth and Planetary Interiors, 143–144, 33–46.

763 Nishihara, Y., Shinmei, T., and Karato, S.I. (2006) Grain-growth kinetics in wadsleyite:
764 Effects of chemical environment. Physics of the Earth and Planetary Interiors, 154, 30–
765 43.

766 Nishihara, Y., Tinker, D., Kawazoe, T., Xu, Y., Jing, Z., Matsukage, K.N., and Karato, S.
767 ichiro (2008) Plastic deformation of wadsleyite and olivine at high-pressure and high-
768 temperature using a rotational Drickamer apparatus (RDA). Physics of the Earth and
769 Planetary Interiors, 170, 156–169.

770 Orear, J. (1982) Least squares when both variables have uncertainties. American Journal of
771 Physics, 50, 912–916.

772 Rios, P.R., and Zöllner, D. (2018) Grain growth–unresolved issues. Materials Science and
773 Technology (United Kingdom), 34, 629–638.

774 Rossouw, D., Burdet, P., De La Peña, F., Ducati, C., Knappett, B.R., Wheatley, A.E.H., and
775 Midgley, P.A. (2015) Multicomponent Signal Unmixing from Nanoheterostructures:

776 Overcoming the Traditional Challenges of Nanoscale X-ray Analysis via Machine
777 Learning. *Nano Letters*, 15, 2716–2720.

778 Saetre, T.O. (2002) On the theory of normal grain growth in two dimensions. *Acta*
779 *Materialia*, 50, 1539–1546.

780 Schneider, C.A., Rasband, W.S., and Eliceiri, K.W. (2012) NIH Image to ImageJ: 25 years of
781 image analysis. *Nature Methods*, 9, 671–675.

782 Soille, P., and Ansuult, M. (1990) Automated basin delineation from {DEM}s using
783 mathematical morphology. *Signal Processing*, 20, 171–182.

784 Solomatov, V.S., and Reese, C.C. (2008) Grain size variations in the Earth’s mantle and the
785 evolution of primordial chemical heterogeneities. *Journal of Geophysical Research*, 113,
786 B07408.

787 Solomatov, V.S., El-Khozondar, R., and Tikare, V. (2002) Grain size in the lower mantle:
788 Constraints from numerical modeling of grain growth in two-phase systems. *Physics of*
789 *the Earth and Planetary Interiors*, 129, 265–282.

790 Stall, S., Yarmey, L., Cutcher-Gershenfeld, J., Hanson, B., Lehnert, K., Nosek, B., Parsons,
791 M., Robinson, E., and Wyborn, L. (2019) Make scientific data FAIR. *Nature*, 570, 27–
792 29.

793 Tsujino, N., and Nishihara, Y. (2009) Grain-growth kinetics of ferropericlasite at high-
794 pressure. *Physics of the Earth and Planetary Interiors*, 174, 145–152.

795 ——— (2010) Effect of pressure on grain-growth kinetics of ferropericlasite to lower mantle
796 conditions. *Geophysical Research Letters*, 37, 1–5.

797 van der Walt, S., Schönberger, J.L., Nunez-Iglesias, J., Boulogne, F., Warner, J.D., Yager,

798 N., Gouillart, E., Yu, T., and the scikit-image contributors (2014) scikit-image: image
799 processing in Python. PeerJ, 2, e453.

800 Wang, W. (2007) Image analysis of size and shape of mineral particles. Proceedings - Fourth
801 International Conference on Fuzzy Systems and Knowledge Discovery, FSKD 2007, 4,
802 41–44.

803 Wright, S.I. (2010) A Parametric Study of Electron Backscatter Diffraction based Grain Size
804 Measurements. Practical Metallography, 47, 16–33.

805 Yamazaki, D., Kato, T., Ohtani, E., and Toriumi, M. (1996) Grain Growth Rates of MgSiO₃
806 Perovskite and Periclase Under Lower Mantle Conditions. Science, 274, 2052–2054.

807 Yamazaki, D., Inoue, T., Okamoto, M., and Irifune, T. (2005) Grain growth kinetics of
808 ringwoodite and its implication for rheology of the subducting slab. Earth and Planetary
809 Science Letters, 236, 871–881.

810 Yamazaki, D., Yoshino, T., Matsuzaki, T., Katsura, T., and Yoneda, A. (2009) Texture of
811 (Mg,Fe)SiO₃ perovskite and ferro-periclase aggregate: Implications for rheology of the
812 lower mantle. Physics of the Earth and Planetary Interiors, 174, 138–144.

813 Yamazaki, D., Matsuzaki, T., Yoshino, T., Suetsugu, D., Bina, C., Inoue, T., Wiens, D., and
814 Jellinek, M. (2010) Grain growth kinetics of majorite and stishovite in MORB. Physics
815 of the Earth and Planetary Interiors, 183, 183–189.

816 Yousefi, J. (2015) Image Binarization using Otsu Thresholding Algorithm. Research Gate.
817